11th International Symposium on Turbulence and Shear Flow Phenomena (TSFP11)
Southampton, UK, July 30 to August 2, 2019

COHERENT STRUCTURE DEFORMATION IN A TURBULENT PIPE FLOW WITH A SPATIALLY-DEVELOPING PRESSURE GRADIENT

Theresa Saxton-Fox[1]
Department of Mechanical and Aerospace Engineering
Princeton University
Princeton, NJ 08544
tsaxtonf@illinois.edu

Liuyang Ding
Department of Mechanical and Aerospace Engineering
Princeton University
Princeton, NJ 08544
liuyangd@princeton.edu

Alexander Smits
Department of Mechanical and Aerospace Engineering
Princeton University
Princeton, NJ 08544
asmits@princeton.edu

Marcus Hultmark
Department of Mechanical and Aerospace Engineering
Princeton University
Princeton, NJ 08544
hultmark@princeton.edu

ABSTRACT

The modification of coherent structures in a turbulent pipe flow was studied as the flow experienced a spatially-varying pressure gradient. The spatially-varying pressure gradient was applied through the inclusion of a body of rotation in the center of the pipe. Particle image velocimetry was carried out in the axial – radial plane for three different bodies of rotation, corresponding to three different spatially-varying pressure gradient profiles. Coherent structures were quantified as the flow spatially evolved by computing two-point correlations centered at different axial locations. A particular contour level of the two-point correlation was chosen and the area within that contour level was computed. The highly-correlated area within the chosen contour level was observed to decrease in the accelerating region of the flow and start to recover back to its initial value when the bulk flow stopped accelerating. The decrease and recovery of the correlated area varied with the size of the body of rotation.

INTRODUCTION

Coherent structures in canonical wall-bounded turbulent flows are commonly used to interpret and understand turbulent physics (Theodorsen, 1952; Robinson, 1991; Jimenez & Moin, 1991; Adrian *et al.*, 2000). They inform theories of how turbulence self-sustains (Jimenez & Moin, 1991), and have acted as building blocks with which turbulence models can be constructed (Perry & Marušic, 1995; Marusic *et al.*, 2010; McKeon, 2017). Many of the structures that have been identified have been common among the three canonical wall-bounded flows (boundary layers, channels, and pipes) within some variation in the exact wavelength (Monty *et al.*, 2009), allowing for some generalizations to be made about structures across these three flows.

When looking towards non-canonical flows, it is therefore natural to look to coherent structures to provide a basis of understanding as well as a potential basis for models. However, coherent structures are known to change non-trivially in both size and strength when the flow undergoes a spatial acceleration. While significant work has looked at the effect of pressure gradients on the statistics of wall-bounded turbulent flows, relatively few works have focused on quantifying the effect on the coherent structures. Early work on the topic was undertaken by Bradshaw (1967), who found that large-scale structures increased in strength in flows with adverse pressure gradients. On the other hand, Spalart & Coleman (1997) showed that the near-wall streaks became weaker in flows with strong adverse pressure gradients, indicating that different scales and different regions of the flow respond differently to pressure gradients.

More recently, Dixit & Ramesh (2010) showed that large scales became more diffuse and elongated and had smaller inclination angles with respect to the wall in a favorable pressure gradient boundary layer. The study was carried out for eight pressure gradient conditions spanning mild to strong. Harun *et al.* (2013) studied the effect of adverse and favorable pressure gradients on large and small scales in a turbulent boundary layer. They found that large scales showed more sensitivity than small scales to pressure gradients. Both of these studies were carried out using hot wires in a boundary layer with a constant pressure gradient along the streamwise extent of the flow within the measurement domain.

Other studies have considered the effect of a spatially-varying pressure gradient and curvature condition on the flow field. Bandyopadhyay & Ahmedt (1993) looked at a sequence of convex and concave geometries as well as the recovery of the flow from these conditions. They found that large eddies responded linearly to increasing pressure gradients, but that the return to equilibrium when the pres-

[1]Present affiliation: Department of Aerospace Engineering University of Illinois at Urbana-Champaign. Urbana, IL 61801

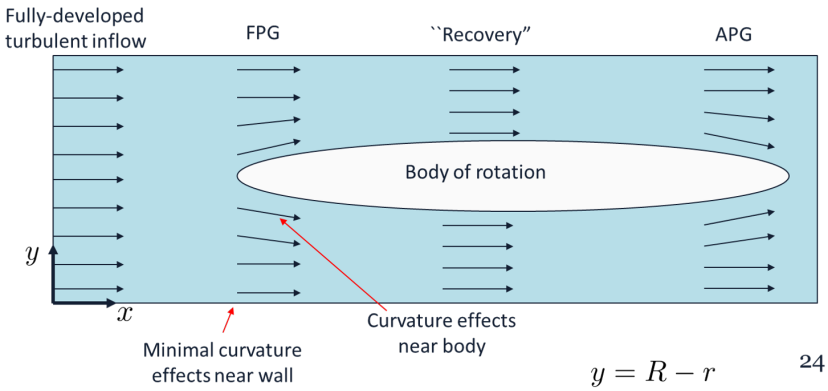

Figure 1: A schematic of the experimental set up is shown. Fully-developed turbulent pipe flow parts around a body of rotation that sits in the center of the pipe.

sure gradient had been withdrawn was nonlinear. Baskaran *et al.* (1987) considered the flow over a curved hill and studied the balance of stress production and dissipation as a result of the pressure gradient and curvature effects. In these flows, the pressure gradient and curvature condition were allowed to vary in the streamwise direction, creating potentially dynamic evolution effects as the velocity field convected through the variable geometry.

In this study, we focus on the effect of a spatially-varying pressure gradient and curvature condition on the strength and size of coherent structures in a turbulent pipe flow. The experimental set up including development of the turbulent pipe flow, creation of the spatially-varying pressure gradient, and measurement of the velocity field using particle image velocimetry are desribed in the experimental methods section. In the results section, two-point correlations are used to deduce the region of strong correlation in the flow field. The area of the strongly-correlated region within a particular contour level is computed and compared as the center point of the two-point correlation is varied and as the size of the body of rotation is changed. Finally, conclusions and a discussion of future work are included in the final section.

EXPERIMENTAL METHOD

The experiment was performed in a recirculating water pipe facility at Princeton University. The water pipe had a diameter of 1.5 ± 0.001 in. A development length of 200 pipe diameters allowed for a fully-developed flow prior to the start of the test section. The facility was capable of a range of Reynolds numbers, $12{,}500 < Re_D < 156{,}000$, and $300 < Re_\tau < 3{,}550$, where $Re_D = U_B D/\nu$, $Re_\tau = u_\tau R/\nu$ and U_B is the bulk axial velocity, u_τ is the friction velocity, D is the diameter of the pipe, R is the radius of the pipe, and ν is the kinematic viscosity. The experiments shown here were run at $Re_D = 156{,}000$ and $Re_\tau = 3{,}550$.

The measurement location was 200 pipe diameters downstream of any pipe bends, such that the inlet flow into the region of interest was a canonical fully-developed turbulent pipe flow. To create a spatially-varying pressure gradient and curvature condition, a body of rotation was held in the center of the pipe using a sting. A schematic of the experiment, showing flow passing by a body of rotation, is shown in figure 1.

Three distinct bodies of rotation were used to generate three different pressure gradient conditions. Each body

Figure 2: The body of rotation is shown outside of the experimental pipe. The sting supporting the body can be observed.

of rotation had the same basic components: a nose cone, a center body, and a tail. In each case, the nose cone was a prolate spheroid, the center body was a cylinder, and the tail was described by a power law, $y^* = R^*(1 - (x^*/L)^4)$, rotated about the axis $y^* = 0$. In the power law, R^* is the maximum radius of the body of rotation and L is the length of the tail component of the body. The difference between the three bodies lay in the radius of the body. The smallest body had a maximum radius of 0.25 in, and filled 1/9 of the area of the pipe. The medium body had a maximum radius of 0.35 in and filled 2/9 of the area of the pipe. The large body had a maximum radius of 0.43 and filled 1/3 of the area of the pipe. An image of the body of rotation held up by its sting and encased in part of the pipe is shown in figure 2. The body of rotation in the full setup is shown in figure 3.

The body shape was chosen with a few design principles in mind. The body was axisymmetric to create a pressure gradient that was varying in the axial direction but not in the azimuthal direction. The nose of the body grew smoothly from a zero-diameter to a maximum diameter to create a smoothly-varying pressure gradient profile. A prolate spheroid was used for the nose as a relatively canonical shape, as it represents an ellipse rotated about its long axis. The center body was chosen to be a cylinder to create a region with no axial variation of the pressure gradient. In this region, the flow is able to recover, albeit in an annular geometry. The tail was described by a power law in order to minimize the separation of the flow (Moonesun *et al.*, 2017). The diameters of the three bodies were chosen such that they filled 1/9, 2/9, and 1/3 of the area of the pipe re-

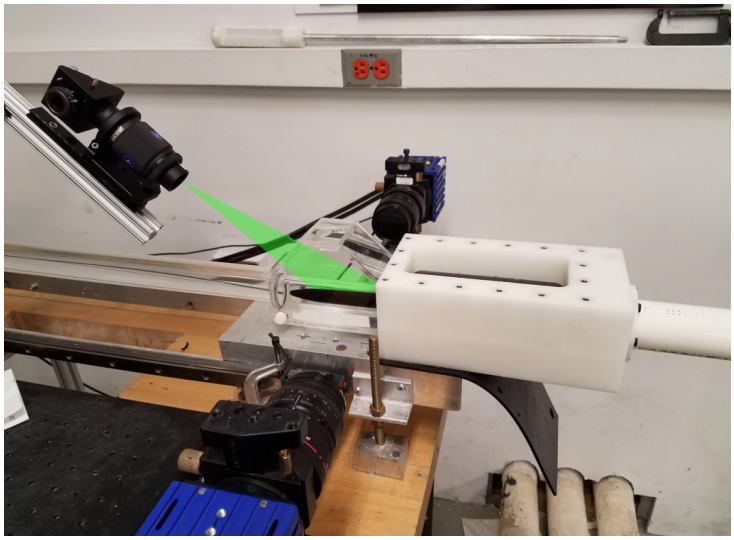

Figure 3: An image of the experimental set up is shown with the body of rotation inside of the glass pipe. The PIV laser sheet is drawn in, and the two PIV cameras are visible. A rectangular box filled with water encasing the pipe is also observable, used to improve the image quality near the walls.

spectively, to generate a wide variety of pressure gradients. The large and small bodies of rotation are shown side-by-side in figure 4. The nose, center body, and tail are visible. The body of revolution was held in the center of the pipe using a sting, with a NACA 0015 shape.

Figure 4: The large and small bodies of rotation are shown side-by-side.

Experiments were carried out for each body of rotation as well as the canonical pipe flow case, in which no body of rotation was included. The velocity field was measured using 2D particle image velocimetry (PIV) in the axial – radial plane. Figure 3 shows the experiment with the PIV laser sheet indicated. A water-filled box was sealed around the pipe at the measurement location in order to reduce image distortion near the curved wall of the pipe. A laser light sheet oriented in the axial – radial plane impinged upon the water-filled box, into the glass measurement pipe. A polarizing filter attached to the camera reduced the effect of laser reflection in the curved glass surfaces. A 2 $\times$ teleconverter was used to magnify the image, such that the final pixel size was $1.85\delta_\nu$ where $\delta_\nu \equiv \nu/u_\tau$. Vector fields were calculated using DaVis software, with a final interrogation spot size of $55\delta_\nu$ and a vector spacing of $27\delta_\nu$.

PIV data was taken in two non-simultaneous experiments to elongate the total field of view. The first set of experiments were undertaken with a field of view starting approximately at the tip of the nose of the body of rotation, extending to approximately 2.75 pipe radii downstream. Two cameras oriented side-by-side were used to achieve this field of view. The second set of experiments were undertaken downstream with a field of view starting approximately at 2.75 pipe radii downstream of the tip of the nose of the body of rotation, and extending to approximately 5.75 pipe radii downstream of the tip of the nose of the body of rotation. Two cameras were again used to achieve this field of view. Thus, four panels make up the field of view of the final results: panels one and two were taken simultaneously and panels three and four were taken simultaneously.

RESULTS

The flow accelerated as it passed by the nose of the body of rotation to conserve mass, creating a favorable pressure gradient throughout the flow and curvature effects in the center of the pipe. The total pressure gradient change based on the geometric variation and associated acceleration for the three bodies of rotation was calculated using the acceleration parameter

$$K(x) \equiv \frac{\nu}{U_b^2(x)} \frac{dU_b(x)}{dx}, \tag{1}$$

where $U_b(x) = Q/(\pi(R^2 - r(x)^2))$, Q is the volumetric flowrate, and r is the local radius of the body of rotation. The value of the acceleration parameter through the axial extent of the field of view is shown in figure 5 for each body of rotation.

The large body's maximum value of K is more than three times larger than the maximum value for the small body, leading to a range of mild to strong pressure gradient values across the three bodies. The small body provides a maximum K value that is consistent with the mild pressure gradient used by Harun *et al.* (2013) and the second

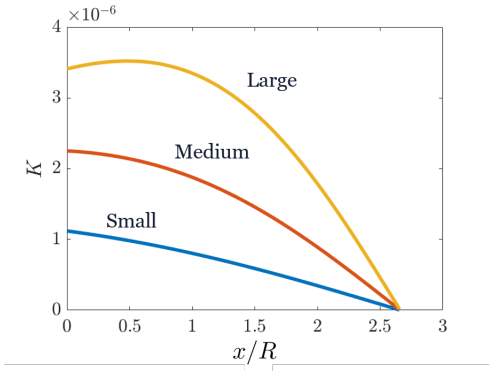

Figure 5: The pressure gradient parameter, K, for each body of rotation is shown, computed based on the bulk flow acceleration required to conserve mass.

pressure gradient of eight (ranked from mild to strong) used by Dixit & Ramesh (2010) in their sweep of the parameter space. The large body provides a maximum K value that is consistent with the seventh pressure gradient of eight used by Dixit & Ramesh (2010), providing a strong pressure gradient locally.

For the case with the medium body of rotation, the resulting mean velocity and the $\overline{uu}$ and $-\overline{uv}$ Reynolds stresses are shown in figure 6 using contour plots to highlight their spatial variation. The values are normalized by the bulk flow in the pipe upstream of the body of rotation, U_B. A more detailed description of the statistical variation is discussed by Ding *et al.* (2019). The present study focuses on the changes of the coherent structures in the flow.

In figure 6, the mean velocity field is observed to globally accelerate, as is required to conserve mass. The Reynolds stresses show decay as the flow accelerates past the nose of the body. This is consistent with previous findings on the decrease in turbulence intensity in favorable pressure gradients (Harun *et al.*, 2013). The Reynolds stresses show signs of recovery as the flow passes the cylindrical center body.

As part of quantifying the change in coherent structures in the flow, we performed two-point correlations at varying axial locations and compared the resulting region of coherence across the different bodies of rotation. Two-point correlations were carried out at a fixed height from the wall $y_0/R = 0.1$ and a set of axial locations $x_0/R = [0.75, 4.5]$, using equation 2. The tip of the nose of the body of rotation defines the zero-point of the axial coordinate.

$$\sigma_{uu}(x,y) = \frac{1}{N}\sum_{t=1}^{N} u(x_0,y_0,t)u(x,y,t), \qquad (2)$$

The velocity field in the two halves of the field of view ($x/R \approx 0-2.75$ and $x/R \approx 2.75-5.5$ respectively) were not measured simultaneously, and therefore the two-point correlations were calculated separately for the two halves. Figure 7 shows a visualization of the two-point correlation carried out at four different values of x_0 for the medium body of rotation. A yellow color in the visualization indicates that the flow is correlated to the central (x_0, y_0) location, while green indicates no correlation. The color bars of the four panels in figure 7 have the same bounds, and make clear that the strength of the correlation declines as the flow passes the nose of the body of rotation and then increases again as the flow passes the cylindrical center body. This is consistent with the decay and recovery of the Reynolds stresses discussed above. The black contour in each panel shows the same value of the two-point correlation, $\sigma_{uu}/U_B^2 = 2.5e-3$.

The area within the highlighted contour level was used to quantify the size and strength of the local coherent structures. A restriction of this method is that, as the chosen point x_0 nears the edges of the domain, some of the true area of the structure becomes occluded. This is visualized to a small degree in figure 7(a) and (d), where parts of the outlined region extend outside of the bounds of the figure. To mitigate this challenge, the two-point correlation was carried out using the same procedure for the canonical turbulent pipe flow and the area within the same contour level was computed. The area of the correlated region for the flow with the body of rotation, A_σ, was normalized by the area of the correlated region for the canonical turbulent pipe flow, $A_{\sigma,0}$, at the same (x_0, y_0) location. Because the structure in the canonical case also extended out of the figure when the x_0 location was too near the edges, the ratio allowed the data to be meaningful for a larger portion of the field of view.

Figure 8 shows the normalized area within the given contour across the three bodies of rotation for a center point height $y_0/R = 0.1$. There are two lines per body of rotation for the two independent fields of view: the usptream half and the downstream half. The value of the contour was chosen as $\sigma_{uu}/U_B^2 = 2.5e-3$. Some artifacts of the limited field of view remain, particularly at the switch from the nose to the center body data, but conclusions can still be deduced.

The area of the correlated region decreases for each body of rotation as the structures pass the nose of the body of rotation. Depending on the size of the body, the behavior for the particular contour level chosen varies significantly. For the large body, the area of the correlated region is already less than 50% of the value for the canonical pipe flow by the time the center point of the two-point correlation enters the field of view, indicating that distortion may begin upstream of the nose of the body. The decrease in area of the given contour level continues until the area is less than 3% of the area for the canonical pipe flow, where it remains between $x/R \approx 2-4$. Just before $x/R \approx 4$, recovery becomes apparent, continuing until the final area ratio returns to about 20% of the value for the canonical pipe flow. For the medium body, the area of the correlated region begins at about 60% of its canonical value and is observed to decrease until $x/R = 2$, at which point the recovery begins immediately. The rate of recovery appears to pick up near the end, again near $x/R = 4$. The final observable value of the ratio of areas is approximately 50% of the canonical value. For the small body, the results are less clear. The initial area is about 70% of the canonical value, and some continued decay is observed up to about $x/R = 1.5$. However, after this point, the results show a complex behavior. The area ratio is observed to vary between about 0.45 and 0.6, showing an increase near the center of the field of view, a decrease around $x/R = 4$, and an increase again near $x/R = 5$. This behavior may indicate a limitation in the analysis method near the edges of the field of view, or may indicate some nonlinear behavior of the structure size. Future work is needed to clarify the result for small pressure gradients and curvatures.

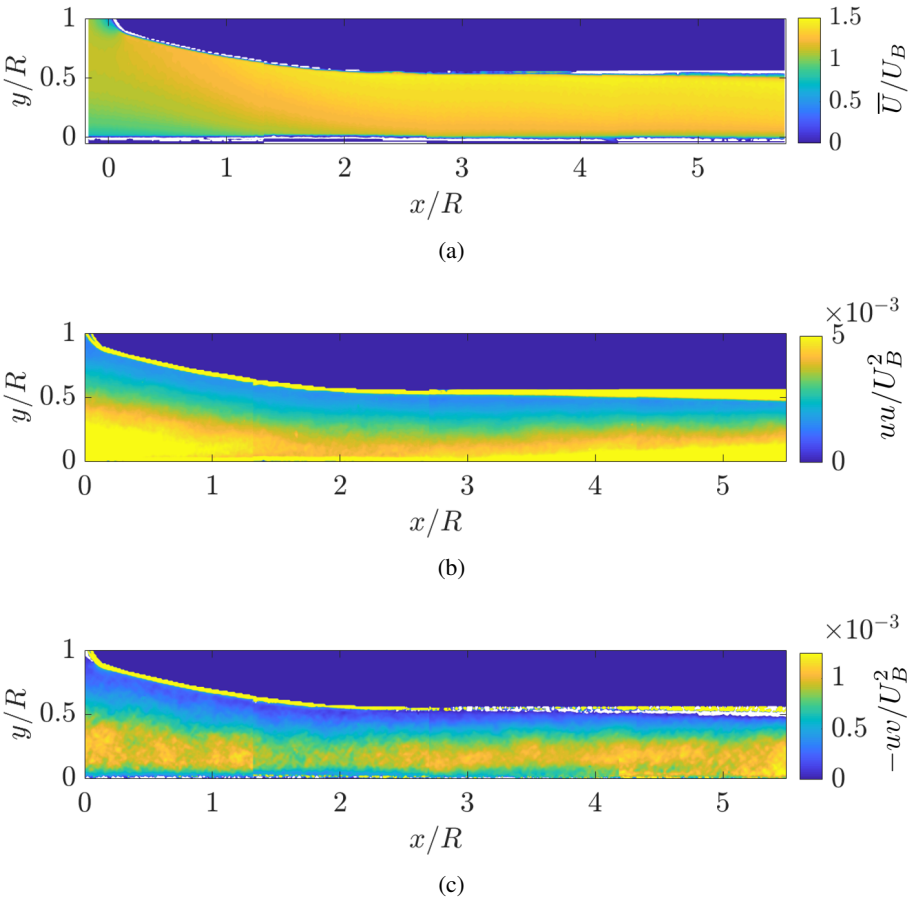

Figure 6: The mean velocity field $\bar{U}$ and Reynolds stresses $\overline{uu}$ and $-\overline{uv}$ for the case with the medium body of rotation. Values are normalized using the bulk velocity upstream of the body of rotation, U_B.

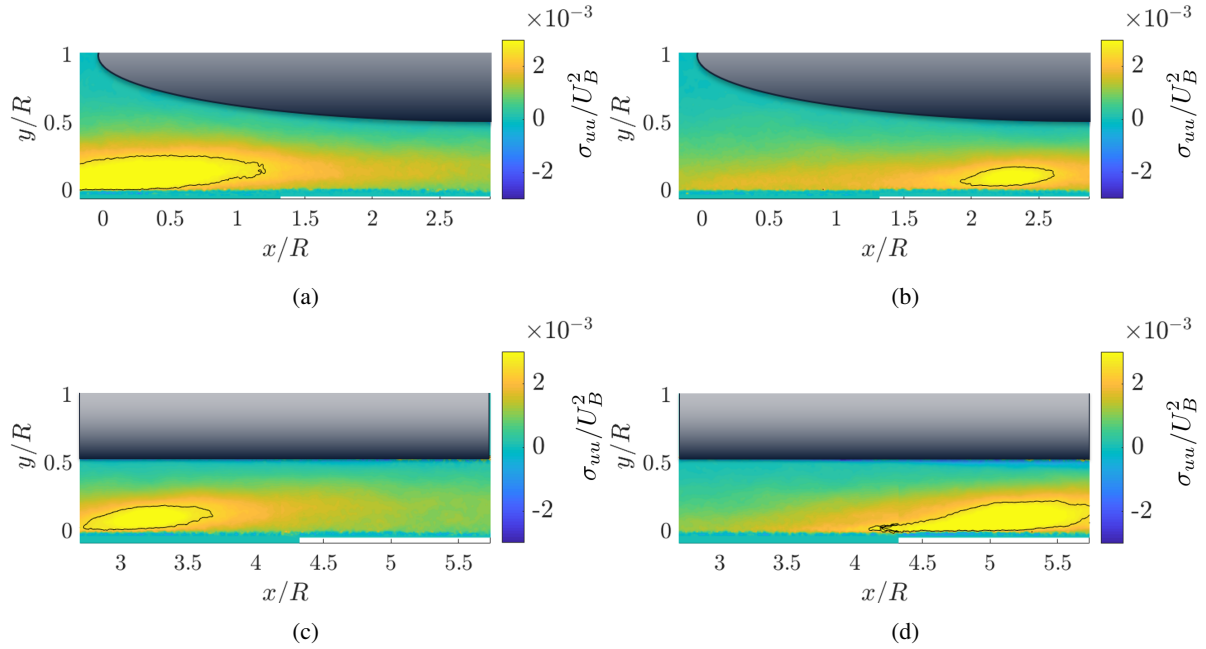

Figure 7: Two-point correlations at four axial locations for the medium body of rotation. A contour level of the same value is outlined in black in each panel to aid comparison.

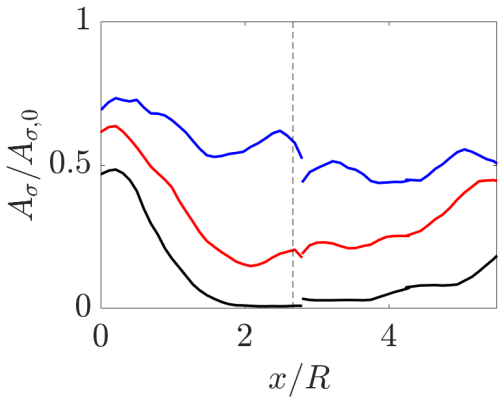

Figure 8: The area of the two-point correlation within a specific contour level. The area variation across the axial extent of the field of view is shown for the case with the small body of rotation (blue), medium body of rotation (red), and large body of rotation (black). The black dashed line indicates the axial location where the nose transitions to the cylindrical center body.

CONCLUSIONS

Experiments were undertaken to measure the variation in the size and strength of coherent structures experiencing a spatially-varying pressure gradient condition. To achieve this goal, three bodies of rotation with varying radii (corresponding to a range of mild to strong acceleration parameters) were held in the center of a pipe and exposed to an incoming canonical turbulent pipe flow. The velocity field was measured using particle image velocimetry as the flow passed the body.

The mean velocity field was observed to accelerate, as was required to conserve mass, while the Reynolds stresses were observed to decay through the bulk acceleration region and start to recover when the acceleration ceased. Two-point correlations were calculated at a number of axial locations and the resulting correlated region was observed to diminish in strength as the flow passed the nose of the body, and increase in strength as the flow passed the cylindrical component of the body.

The change in the two-point correlations was quantified by calculating the area within a fixed contour level across the axial direction of the flow and across the three bodies of rotation. The area within a given contour level was observed to decay for all three conditions, though the rate and extent of the decay was larger for the larger bodies of rotation. A clear pattern of decreasing area in the accelerating region and increasing area in the recovery region was observed for the medium and large bodies, while the small body showed more complex behavior requiring further inquiry.

This work contributes to the goal of quantifying the continuous deformation of coherent structures when they are exposed to complex changes of geometry. Future work will seek to tie these structural changes to the local acceleration parameter and bulk flow condition, towards a clear relationship between the external flow condition and the local structural behavior.

Acknowledgements

The authors gratefully acknowledge the support of ONR Grant N00014-17-1-2309 through Program Manager Joseph Gorski, which enabled the execution of this research.

REFERENCES

Adrian, R J, Meinhart, C D & Tomkins, C D 2000 Vortex organization in the outer region of the turbulent boundary layer. *Journal of Fluid Mechanics* **422**, 1–54.

Bandyopadhyay, Promode R. & Ahmedt, Anwar 1993 Turbulent boundary layers subjected to multiple curvatures and pressure gradients. *Journal of Fluid Mechanics* **246**, 503–527.

Baskaran, V., Smits, A.J. & Joubert, P.N. 1987 A turbulent flow over a curved hill - Part 1. Growth of an internal boundary layer. *Journal of Fluid Mechanics* **182**, 47–83.

Bradshaw, P. 1967 The turbulence structure of equilibrium boundary layers. *Journal of Fluid Mechanics* **29** (4), 625–645.

Ding, L., Saxton-Fox, T., Smits, L. & Hultmark, M. 2019 No Title. In *Turbulent Shear Flow Phenomena*.

Dixit, Shivsai Ajit & Ramesh, O. N. 2010 *Large-scale structures in turbulent and reverse-transitional sink flow boundary layers*, , vol. 649.

Harun, Zambri, Monty, Jason P., Mathis, Romain & Marusic, Ivan 2013 Pressure gradient effects on the large-scale structure of turbulent boundary layers. *Journal of Fluid Mechanics* **715**, 477–498.

Jimenez, J & Moin, P 1991 The minimal flow unit in near-wall turbulence. *Journal of Fluid Mechanics* **225**, 213–240.

Marusic, I, Mathis, R & Hutchins, N 2010 Predictive Model for Wall-Bounded Turbulent Flow. *Science* **329** (5988), 193–196.

McKeon, B J 2017 The engine behind (wall) turbulence: perspectives on scale interactions. *Journal of Fluid Mechanics* **817**.

Monty, J P, Hutchins, N, Ng, H C H, Marusic, I & Chong, M S 2009 A comparison of turbulent pipe, channel and boundary layer flows. *Journal of Fluid Mechanics* **632**, 431–442.

Moonesun, Mohammad, Korol, Yuri Mikhailovich, Dalayeli, Hosein, Tahvildarzade, Davood, Javadi, Mehran, Jelokhaniyan, Mohammad & Mahdian, Asghar 2017 Optimization on submarine stern design. *Proceedings of the Institution of Mechanical Engineers Part M: Journal of Engineering for the Maritime Environment* **231** (1), 109–119.

Perry, A. E. & Marušic, Ivan 1995 A wall-wake model for the turbulence structure of boundary layers. Part 1. Extension of the attached eddy hypothesis. *Journal of Fluid Mechanics* **298** (-1), 361.

Robinson, S K 1991 Coherent motions in the turbulent boundary layer. *Annual Review of Fluid Mechanics* **23**, 601–639.

Spalart, P.R. & Coleman, G.N. 1997 No Title. *European Journal of Mechanics* **16** (2), 169–189.

Theodorsen, T 1952 Mechanism of turbulence. In *Proceedings of the Midwestern Conference on Fluid Mechanics*. Ohio State University, Columbus, OH.